From continuous to discontinuous failure in a gradient-enhanced continuum damage model

Angelo Simone [1], Garth N. Wells [*,2], Lambertus J. Sluys

Faculty of Civil Engineering and Geosciences, Delft University of Technology, P.O. Box 5048, 2600 GA Delft, The Netherlands

Abstract

A computational framework for the description of the combined continuous–discontinuous failure in a regularised strain-softening continuum is proposed. The continuum is regularised through the introduction of gradient terms into the constitutive equations. At the transition to discrete failure, the problem fields are enhanced through a discontinuous interpolation based on the partition of unity paradigm of finite-element shape functions. The inclusion of internal discontinuity surfaces, where boundary conditions are applied without modifications of the original finite-element mesh, avoids the unrealistic damage growth typical of this class of regularised continuum models. Combined models allow for the analysis of the entire failure process, from diffuse microcracking to localised macrocracks. The discretisation procedure is described in detail and numerical examples illustrate the performance of the combined continuous–discontinuous approach.
© 2003 Elsevier B.V. All rights reserved.

Keywords: Gradient-enhanced continuum; Non-local continuum; Partition of unity; Enriched finite-elements; Discontinuities; Fracture; Damage

1. Introduction

Failure of most engineering materials is a phenomenon characterised by the development of a process zone in which microcracks arise, deformations localise and the accumulation of damage eventually leads to traction-free macrocracks with eventual total loss of load-carrying capacity. A computational framework for the realistic description of any failure process must describe the initial as well the final stage of failure in a unified fashion.

Computational approaches to failure have traditionally used two distinct concepts: fracture mechanics and damage mechanics. The former falls in the family of discrete or discontinuous models while the latter belongs to the family of continuous models. Fracture mechanics analyses, based on the cohesive zone model

---

[9], have been restricted in their applications due to the traditional formulation of the finite-element method which requires that discontinuities are prescribed to propagate along pre-defined element boundaries. This can be overcome by using remeshing techniques [11,20], by embedding cohesive surfaces along all possible element boundaries [29,34] or by a discontinuous interpolation of the displacement field [19,32]. However, discontinuous models cannot adequately capture diffuse degradation, when used with an elastic continuum. Unlike fracture mechanics approaches, damage mechanics analyses can reasonably represent diffuse degradation but, due to the introduction of strain-softening relationships, suffer from lack of objectivity with respect to spatial discretisation, originating from an inadequate underlying mathematical description. Objectivity of the numerical model at the onset of localisation can be maintained through introduction of non-local interactions [2,3,25,26]. However, despite the regularisation, the response of standard non-local continuum damage models, in either integral [26] or differential [25] format, deteriorates in the final stage of failure due to spurious damage growth as the models are unable to represent discrete failure surfaces [6].

The basic idea proposed in this work is to combine the two failure descriptions to achieve a better characterisation of failure and, at the same time, to avoid spurious damage growth. To this end, a regularised continuum model will be coupled to a discontinuous model. The use of a combined fracture/damage mechanics approach was advocated in Ref. [12] as a way to achieve a more realistic assessment of the bearing capacity of a loaded structure while the transition from a regularised continuum model to discrete cracking was analysed in Ref. [14] using embedded discontinuities.

The recently re-assessed partition of unity requirement of finite-element interpolations [5,16] has allowed the inclusion of arbitrary enrichments in the interpolation of the problem fields in a natural fashion. The inclusion of a discontinuous enrichment in the problem fields was proposed in a fracture mechanics context [19] to simulate traction-free cracks in elastic bodies without alteration of mesh topology; this approach has been extended to simulate the propagation of cohesive cracks in a classical continuum [18,32] and of traction-free cracks in a regularised viscoplastic strain-softening continuum [33].

In this work, the introduction of traction-free discontinuities in a differential version of a non-local damage model is presented. Discontinuities are introduced when the material reaches a fully damaged state. By introducing a discontinuity, non-local interactions across the crack cease and the unbounded strain on the surface has no influence on the non-local field. After the introduction of a discontinuity in the problem fields, coupling between fully damaged locations and the surrounding material ceases and damage away from the discontinuity tip is frozen; additional degradation is described by the damaging material in the process zone, around the discontinuity tip. It is shown that through the introduction of discontinuities in a gradient damage model, spurious damage growth is avoided and a more realistic description of the entire failure process, from diffuse microcracking to macroscopic traction-free cracks, can be achieved.

2. Problem fields

When a body is crossed by a discontinuity, it is necessary to characterise the problem fields in a proper way. In the regularised continuum model here used, a gradient-enhanced damage continuum model [25], the problem is described by the displacement field $\mathbf{u}$ and by the scalar non-local equivalent strain field e.

2.1. Discontinuous problem fields

The body $\bar{\Omega}$, depicted in Fig. 1, is bounded by Γ and is crossed by a discontinuity surface Γ_d which divides the body into two sub-domains, Ω^+ and Ω^- ($\Omega = \Omega^+ \cup \Omega^-$). The boundary surface of the body $\bar{\Omega}$ consists of three mutually disjoint boundary surfaces, Γ_u, Γ_t and Γ_d ($\Gamma = \Gamma_u \cup \Gamma_t$). Displacements $\bar{\mathbf{u}}$ are prescribed on Γ_u, while tractions $\bar{\mathbf{t}}$ are prescribed on Γ_t. In the body $\bar{\Omega}$, the displacement field can be decomposed as
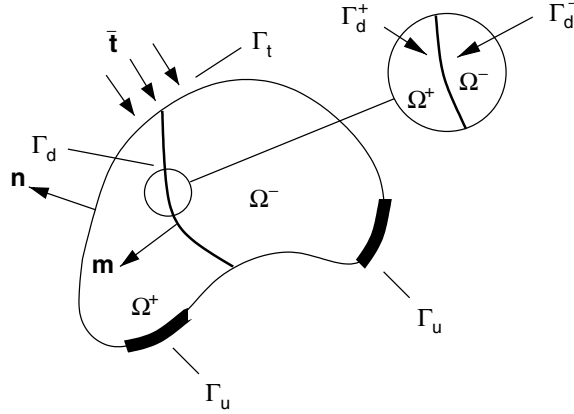
Fig. 1. Body $\bar{\Omega}$ crossed by a discontinuity Γ_d.

$$\mathbf{u}(\mathbf{x},t) = \hat{\mathbf{u}}(\mathbf{x},t) + \mathscr{H}_{\Gamma_\mathrm{d}}(\mathbf{x})\tilde{\mathbf{u}}(\mathbf{x},t), \tag{1}$$

where $\mathscr{H}_{\Gamma_\mathrm{d}}(\mathbf{x})$ is the Heaviside function centred at the discontinuity surface Γ_d ($\mathscr{H}_{\Gamma_\mathrm{d}} = 1$ if $\mathbf{x} \in \bar{\Omega}^+$, $\mathscr{H}_{\Gamma_\mathrm{d}} = 0$ if $\mathbf{x} \in \bar{\Omega}^-$) and $\hat{\mathbf{u}}$ and $\tilde{\mathbf{u}}$ are continuous functions on $\bar{\Omega}$. A similar decomposition holds for the non-local equivalent strain field:

$$e(\mathbf{x},t) = \hat{e}(\mathbf{x},t) + \mathscr{H}_{\Gamma_\mathrm{d}}(\mathbf{x})\tilde{e}(\mathbf{x},t), \tag{2}$$

where $\hat{e}$ and $\tilde{e}$ are continuous functions on $\bar{\Omega}$. In the geometrically linear case, the strain field in Ω is computed as the symmetric part of the gradient of the displacement field, which yields

$$\boldsymbol{\varepsilon}(\mathbf{x},t) = \mathbf{V}^\mathrm{s}\hat{\mathbf{u}}(\mathbf{x},t) + \mathscr{H}_{\Gamma_\mathrm{d}}(\mathbf{x})\mathbf{V}^\mathrm{s}\tilde{\mathbf{u}}(\mathbf{x},t) \quad \text{if } \mathbf{x} \notin \Gamma_\mathrm{d}, \tag{3}$$

where $(\cdot)^\mathrm{s}$ refers to the symmetric part of $(\cdot)$. Note that Eq. (2) can be derived by direct substitution of the local strain field from Eq. (3) into the non-local averaging operator (see Ref. [26] for its definition). The decomposition in Eq. (2) can be considered as a a direct consequence of the definition of the strain field in Eq. (3).

2.2. Interpolation of discontinuous fields

Discontinuities in the problem fields can be introduced by using the partition of unity paradigm of finite-element shape functions [19]. The 'effect' of a discontinuity is added to the problem fields in terms of an enhancement, affecting only nodes whose support is crossed by a discontinuity. Following Ref. [32], in the domain of an element where enhanced nodes are active, an approximation of the displacement field in Eq. (1) is given by

$$\mathbf{u}_h = \mathbf{N}\mathbf{a} + \mathscr{H}_{\Gamma_\mathrm{d}}\mathbf{N}\mathbf{b}, \tag{4}$$

where the global nodal degrees of freedom $\mathbf{a}$ and $\mathbf{b}$ represent, in the arrangement of Eq. (4), the total displacement field; the displacement jump across the discontinuity Γ_d is given by

$$[\![\mathbf{u}_h]\!] = \mathbf{N}\mathbf{b}|_{\Gamma_\mathrm{d}}. \tag{5}$$

Similar considerations hold for the approximations of the strain field and the non-local equivalent strain field. For nodes whose support is not crossed by a discontinuity, the Heaviside function is a constant

function over their supports and therefore it is not considered. Consequently, since there is no enhancement, the standard finite-element interpolation $\mathbf{u}_h = \mathbf{Na}$ is retrieved.

3. Problem statement

The equilibrium equations and boundary conditions for the body $\bar{\Omega}$ without body forces are summarised by

$$\nabla \cdot \boldsymbol{\sigma} = \mathbf{0} \quad \text{in } \Omega, \tag{6}$$

$$\boldsymbol{\sigma}\mathbf{n} = \bar{\mathbf{t}} \quad \text{on } \Gamma_t, \tag{7}$$

$$\boldsymbol{\sigma}\mathbf{m} = \mathbf{t} \quad \text{on } \Gamma_d, \tag{8}$$

where $\boldsymbol{\sigma}$ is the Cauchy stress tensor and the last equation represents traction continuity at the discontinuity surface Γ_d with $\mathbf{m}$ as the direction normal to the discontinuity (see Fig. 1). In this contribution, a discontinuity stems as a consequence of complete material failure. Consequently, only traction-free discontinuities are considered (i.e. $\mathbf{t} = \mathbf{0}$ in Eq. (8)). The strong form is completed by the essential boundary condition

$$\mathbf{u} = \bar{\mathbf{u}} \quad \text{on } \Gamma_u, \tag{9}$$

where $\bar{\mathbf{u}}$ is a prescribed displacement, and by the constitutive relation for the elasticity-based isotropic description of continuum damage:

$$\boldsymbol{\sigma} = (1 - \omega)\mathbf{D} : \boldsymbol{\varepsilon} \quad \text{in } \Omega \tag{10}$$

in which ω is the isotropic damage parameter ($0 \leqslant \omega \leqslant 1$), function of the monotonically increasing deformation history parameter κ, $\mathbf{D}$ is the fourth-order constitutive elasticity tensor and $\boldsymbol{\varepsilon}$ is the strain tensor. The evolution of the history parameter κ is governed by the Kuhn–Tucker relations:

$$\dot{\kappa} \geqslant 0, \quad e - \kappa \leqslant 0, \quad \dot{\kappa}(e - \kappa) = 0, \tag{11}$$

where e is the non-local equivalent strain. Damage evolution can be described by using an exponential softening law [15,25]:

$$\omega = \begin{cases} 0 & \text{if } \kappa \leqslant \kappa_0, \\ 1 - \dfrac{\kappa_0}{\kappa}(1 - \alpha + \alpha e^{-\beta(\kappa - \kappa_0)}) & \text{if } \kappa > \kappa_0 \end{cases} \tag{12}$$

with α and β model parameters and κ_0 the threshold for damage initiation, or by a modified power softening law [6]:

$$\omega = \begin{cases} 0 & \text{if } \kappa < \kappa_0, \\ 1 - \left(\dfrac{\kappa_0}{\kappa}\right)^{\beta}\left(\dfrac{\kappa_c - \kappa}{\kappa_c - \kappa_0}\right)^{\alpha} & \text{if } \kappa_0 \leqslant \kappa \leqslant \kappa_c, \\ 1 & \text{if } \kappa > \kappa_c, \end{cases} \tag{13}$$

where κ_c represents the value of κ for which damage reaches unity and model parameters α and β influence the slope and the shape of the softening curve, respectively.

The differential format of the non-local integral averaging of the local equivalent strain ε_{eq} results in a modified Helmholtz equation for the non-local equivalent strain e [25]:

$$e - c\nabla^2 e = \varepsilon_{eq} \quad \text{in } \Omega, \tag{14}$$

where c is the gradient parameter (related to the length scale through $c = \frac{1}{2}l^2$), which, together with the homogeneous natural boundary condition

$$\mathbf{\nabla}e \cdot \mathbf{n} = 0 \quad \text{on } \Gamma, \tag{15}$$

completes the coupled system of equations. The equivalent strain ε_{eq} in Eq. (14) can be expressed through the modified von Mises definition [22,30]:

$$\varepsilon_{\text{eq}} = \frac{k-1}{2k(1-2v)}I_1 + \frac{1}{2k}\sqrt{\frac{(k-1)^2}{(1-2v)^2}I_1^2 - \frac{12k}{(1+v)^2}J_2} \tag{16}$$

with I_1 and J_2 the first invariant of the strain tensor and the second invariant of the deviatoric strain tensor, respectively, k the ratio of the compressive and tensile strength and v the Poisson's ratio. An alternative expression for the equivalent strain ε_{eq} is based on the positive principal strain components $\langle \varepsilon_i \rangle$ [15]:

$$\varepsilon_{\text{eq}} = \sqrt{\sum_{i=1,2,3} \langle \varepsilon_i \rangle^2}. \tag{17}$$

From the decomposition of the non-local equivalent strain e in Eq. (2) and using Eq. (15), the boundary conditions at the discontinuity surface Γ_{d} (see Fig. 1) can be written as:

$$\mathbf{\nabla}\hat{e} \cdot \mathbf{m} = 0 \quad \text{on } \Gamma_{\text{d}}^-, \tag{18}$$

$$\mathbf{\nabla}(\hat{e} + \tilde{e}) \cdot \mathbf{m} = 0 \quad \text{on } \Gamma_{\text{d}}^+. \tag{19}$$

Since the function $\hat{e}$ is a continuous function, $\hat{e}^+ = \hat{e}^-$, where $\hat{e}^{+/-}$ indicates the value of $\hat{e}$ on $\Gamma_{\text{d}}^{+/-}$. Therefore,

$$(\mathbf{\nabla}\hat{e} \cdot \mathbf{m})|_{\Gamma_{\text{d}}^+} = (\mathbf{\nabla}\hat{e} \cdot \mathbf{m})|_{\Gamma_{\text{d}}^-} = 0. \tag{20}$$

From Eqs. (19) and (20), it follows that $\mathbf{\nabla}\tilde{e} \cdot \mathbf{m} = 0$ on Γ_{d}^+. In summary, the boundary conditions for the non-local equivalent strain e at the discontinuity surface are:

$$\mathbf{\nabla}\hat{e} \cdot \mathbf{m} = 0 \quad \text{on } \Gamma_{\text{d}}^{+/-}, \tag{21}$$

$$\mathbf{\nabla}\tilde{e} \cdot \mathbf{m} = 0 \quad \text{on } \Gamma_{\text{d}}^+. \tag{22}$$

3.1. Propagating discontinuities and boundary conditions

Together with the boundary conditions for the displacement fields, the above boundary conditions allow the development of the process zone into a macroscopic crack. Indeed, Eq. (14) is only valid on the domain $\tilde{\Omega} = \Omega_{\text{e}} \cup \Omega_{\text{p}}$ (see Fig. 2) of the body where $0 \leqslant \omega < 1$. Since the process zone Ω_{p} and the fully damaged domain Ω_{d} will increase during a computation, the numerical procedure must consider the evolution of the internal boundary Γ_{d}.

The evolution of the fully damaged zone can be dealt with by modifying the domain of the problem (using remeshing and adaptive techniques or removing fully damaged elements as done in Refs. [22,24]). To avoid singularities in the system due to $\omega = 1$, exponential-like softening laws (see Eq. (12)) can be used. In this way, the damaging body will never experience full damage.

This may sound appealing from the numerical point of view in the sense that it is then possible to perform computations in a continuous framework and consider as fully damaged zones those parts of the body where damage is close to unity. However, since in those parts of the body the non-local equivalent strain reaches extremely high values, due to the non-local averaging either integral or differential damage
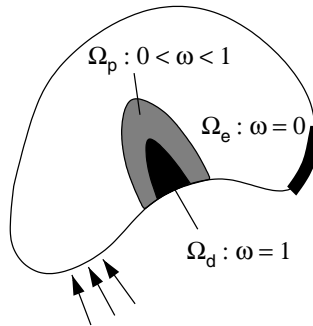
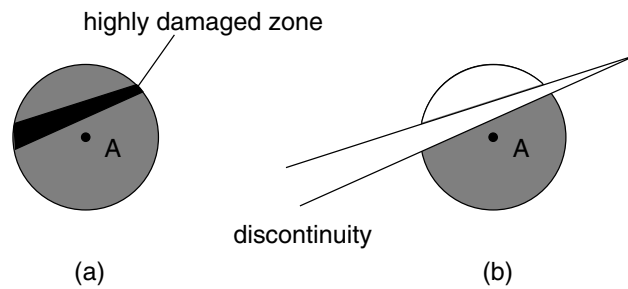Fig. 2. Damage distribution in a continuum (adapted from Ref. [22]).

Fig. 3. Non-local averaging for point A close to a numerical macrocrack (highly damaged locations) in the darker area: (a) a standard non-local model averages *on* and *across* the numerical macrocrack while (b) the non-local averaging is limited to the shaded part when a true discontinuity is present (adapted from Ref. [31]).

models transfer information from physically fully damaged zones to partly damaged zones, resulting in spurious damage growth away from the discontinuity tip [6]. With the combined continuous–discontinuous description of failure, the incorporation of the standard boundary conditions for the problem fields where damage has reached its critical value is automatic and allows the development of boundary surfaces. The application of the standard boundary conditions to $\mathbf{u}$ and e on the internal boundary surfaces alters the averaging procedure and implies that the non-local averaging for point A in Fig. 3b is limited to the shaded part only. Classical non-local models are unable to detect a numerical macrocrack (highly damaged locations) and non-local averaging for point A is performed *across* and *on* the numerical macrocrack (see Fig. 3a) with consequent spurious damage growth.

4. Variational formulation

In this section, following standard procedures, the governing system of coupled partial differential equations of the combined continuous–discontinuous gradient-enhanced damage model will be cast in a weak form. The space of trial displacements is defined by the function $\mathbf{u}(\mathbf{x}, t) = \hat{\mathbf{u}}(\mathbf{x}, t) + \mathscr{H}_{\Gamma_d}\tilde{\mathbf{u}}(\mathbf{x}, t)$ with $\hat{\mathbf{u}}$ and $\tilde{\mathbf{u}} \in U_u$ where

$$U_u = \{\hat{u}_i \text{ and } \tilde{u}_i \mid \hat{u}_i \text{ and } \tilde{u}_i \in H^1(\Omega) \text{ and } \hat{u}_i|_{\Gamma_u} = \bar{u}_i, \ \tilde{u}_i|_{\Gamma_u} = 0\} \tag{23}$$

with H^1 a Sobolev space; $\hat{u}_i$ and $\tilde{u}_i$ indicate the *i*th component of $\hat{\mathbf{u}}$ and $\tilde{\mathbf{u}}$, respectively. The space of admissible displacement variations is defined by the weight function $\mathbf{w}_u(\mathbf{x}) = \hat{\mathbf{w}}_u(\mathbf{x}) + \mathscr{H}_{\Gamma_\mathrm{d}}\tilde{\mathbf{w}}_u(\mathbf{x})$ with $\hat{\mathbf{w}}_u$ and $\tilde{\mathbf{w}}_u \in W_{u,0}$ where

$$W_{u,0} = \{\hat{w}_{u,i} \text{ and } \tilde{w}_{u,i} \mid \hat{w}_{u,i} \text{ and } \tilde{w}_{u,i} \in H^1(\Omega) \text{ and } \hat{w}_{u,i}|_{\Gamma_u} = \tilde{w}_{u,i}|_{\Gamma_u} = 0\}, \tag{24}$$

where $\hat{w}_{u,i}$ and $\tilde{w}_{u,i}$ indicate the *i*th component of $\hat{\mathbf{w}}_u$ and $\tilde{\mathbf{w}}_u$, respectively. In an analogous fashion, the space of trial non-local equivalent strains is defined by the function $e(\mathbf{x}, t) = \hat{e}(\mathbf{x}, t) + \mathscr{H}_{\Gamma_\mathrm{d}}\tilde{e}(\mathbf{x}, t)$ with $\hat{e}$ and $\tilde{e} \in H^1(\Omega)$ while the space of admissible non-local equivalent strain variations is defined by the weight function $w_e(\mathbf{x}) = \hat{w}_e(\mathbf{x}) + \mathscr{H}_{\Gamma_\mathrm{d}}\tilde{w}_e(\mathbf{x})$ with $\hat{w}_e$ and $\tilde{w}_e \in H^1(\Omega)$.

The equilibrium equations (see Eq. (6)) are multiplied by the weight function $\mathbf{w}_u \in W_{u,0}$, which is decomposed into $\hat{\mathbf{w}}_u$ and $\tilde{\mathbf{w}}_u$ consistent with the displacement decomposition in Eq. (1), and integrated over the domain Ω to obtain a weak equilibrium statement. Following standard procedures and using the additional condition $\tilde{\mathbf{u}} = \mathbf{0}$ on Γ_u for the magnitude of the displacement jump [32] leads to two variational statements:

$$\int_\Omega \mathbf{V}^\mathrm{s}\hat{\mathbf{w}}_u : \boldsymbol{\sigma}\,\mathrm{d}\Omega = \int_{\Gamma_t} \hat{\mathbf{w}}_u \cdot \bar{\mathbf{t}}\,\mathrm{d}\Gamma \quad \forall\hat{\mathbf{w}}_u \in W_{u,0}, \tag{25a}$$

$$\int_{\Omega^+} \mathbf{V}^\mathrm{s}\tilde{\mathbf{w}}_u : \boldsymbol{\sigma}\,\mathrm{d}\Omega = \int_{\Gamma_t^+} \tilde{\mathbf{w}}_u \cdot \bar{\mathbf{t}}\,\mathrm{d}\Gamma \quad \forall\tilde{\mathbf{w}}_u \in W_{u,0}. \tag{25b}$$

Compared to the variational statement related to a body under a continuous kinematic field,

$$\int_\Omega \mathbf{V}^\mathrm{s}\mathbf{w}_u : \boldsymbol{\sigma}\,\mathrm{d}\Omega = \int_{\Gamma_t} \mathbf{w}_u \cdot \bar{\mathbf{t}}\,\mathrm{d}\Gamma \quad \forall\mathbf{w}_u \in H_0^1(\Omega). \tag{26}$$

Eq. (25) can be understood as the virtual work expressions for the body $\bar{\Omega}$ under the continuum displacement field $\hat{\mathbf{u}}$ and for the body $\bar{\Omega}^+$ under the displacement field $\mathscr{H}_{\Gamma_\mathrm{d}}\tilde{\mathbf{u}}$.

In a similar fashion, Eq. (14) for the non-local equivalent strain can be recast in a variational form by multiplying it by a scalar weight function $w_e \in H^1(\Omega)$ (split into $\hat{w}_e$ and $\tilde{w}_e$) and by integrating over the domain Ω. The weak form of the modified Helmholtz equation reads:

$$\int_\Omega (\hat{w}_e + \mathscr{H}_{\Gamma_\mathrm{d}}\tilde{w}_e)(\hat{e} + \mathscr{H}_{\Gamma_\mathrm{d}}\tilde{e})\,\mathrm{d}\Omega - c\int_\Omega (\hat{w}_e + \mathscr{H}_{\Gamma_\mathrm{d}}\tilde{w}_e)\nabla^2(\hat{e} + \mathscr{H}_{\Gamma_\mathrm{d}}\tilde{e})\,\mathrm{d}\Omega$$

$$= \int_\Omega (\hat{w}_e + \mathscr{H}_{\Gamma_\mathrm{d}}\tilde{w}_e)\varepsilon_\mathrm{eq}\,\mathrm{d}\Omega \quad \forall w_e \in H^1(\Omega). \tag{27}$$

From the decomposition of the problem fields it follows that any admissible variation w_e of e can be regarded as admissible variations $\hat{w}_e$ and $\tilde{w}_e$, thus leading to two variational statements. Taking first variations $\hat{w}_e$ ($\tilde{w}_e = 0$), and then $\tilde{w}_e$ ($\hat{w}_e = 0$), leads to:

$$\int_\Omega \hat{w}_e(\hat{e} + \mathscr{H}_{\Gamma_\mathrm{d}}\tilde{e})\,\mathrm{d}\Omega - c\int_\Omega \hat{w}_e\nabla^2(\hat{e} + \mathscr{H}_{\Gamma_\mathrm{d}}\tilde{e})\,\mathrm{d}\Omega = \int_\Omega \hat{w}_e\varepsilon_\mathrm{eq}\,\mathrm{d}\Omega \quad \forall\hat{w}_e \in H^1(\Omega), \tag{28a}$$

$$\int_\Omega \mathscr{H}_{\Gamma_\mathrm{d}}\tilde{w}_e(\hat{e} + \mathscr{H}_{\Gamma_\mathrm{d}}\tilde{e})\,\mathrm{d}\Omega - c\int_\Omega \mathscr{H}_{\Gamma_\mathrm{d}}\tilde{w}_e\nabla^2(\hat{e} + \mathscr{H}_{\Gamma_\mathrm{d}}\tilde{e})\,\mathrm{d}\Omega = \int_\Omega \mathscr{H}_{\Gamma_\mathrm{d}}\tilde{w}_e\varepsilon_\mathrm{eq}\,\mathrm{d}\Omega \quad \forall\tilde{w}_e \in H^1(\Omega). \tag{28b}$$

Using the product rule for the Laplacian of a discontinuous scalar field, the term $\nabla^2(\mathscr{H}_{\Gamma_\mathrm{d}}\phi)$ in the previous equations is equal to:

$$\nabla^2(\mathscr{H}_{\Gamma_\mathrm{d}}\phi) = \mathscr{H}_{\Gamma_\mathrm{d}}\nabla^2\phi + \phi\mathbf{V}\delta_{\Gamma_\mathrm{d}} \cdot \mathbf{m} + 2\delta_{\Gamma_\mathrm{d}}\mathbf{V}\phi \cdot \mathbf{m}, \tag{29}$$

where δ_{Γ_d} is the Dirac-delta function centred at the discontinuity surface Γ_d. Substitution of the above relation into Eq. (28) leads to terms of the type $\int_{\Omega} \phi \mathbf{V} \delta_{\Gamma_d} \cdot \mathbf{m} \, d\Omega$ which can be expanded using the directional derivative of a function ϕ in the direction of a generic unit vector $\mathbf{v}$ ($D_{\mathbf{v}}\phi = \mathbf{V}\phi \cdot \mathbf{v}$):

$$\int_{\Omega} (\mathbf{V}\delta_{\Gamma_d} \cdot \mathbf{v})\phi \, d\Omega = \int_{\Omega} D_{\mathbf{v}}\delta_{\Gamma_d} \phi \, d\Omega = -\int_{\Gamma_d} D_{\mathbf{v}}\phi \, d\Gamma = -\int_{\Gamma_d} \mathbf{V}\phi \cdot \mathbf{v} \, d\Gamma. \tag{30}$$

Note that Eq. (30) has been derived using the following relation for the Dirac-delta function δ_{Γ_d} [28]:

$$\int_{\Omega} (\mathbf{V}\delta_{\Gamma_d})\phi \, d\Omega = -\int_{\Gamma_d} \mathbf{V}\phi \, d\Gamma. \tag{31}$$

Using Green's theorem and after the application of the boundary conditions, the variational statements in Eq. (28) can be written as:

$$\int_{\Omega} \hat{w}_e \hat{e} \, d\Omega + \int_{\Omega^+} \hat{w}_e \tilde{e} \, d\Omega + c \int_{\Omega} \mathbf{V}\hat{w}_e \cdot \mathbf{V}\hat{e} \, d\Omega + c \int_{\Omega^+} \mathbf{V}\hat{w}_e \cdot \mathbf{V}\tilde{e} \, d\Omega = \int_{\Omega} \hat{w}_e \varepsilon_{eq} \, d\Omega \quad \forall \hat{w}_e \in H^1(\Omega), \tag{32a}$$

$$\int_{\Omega^+} \tilde{w}_e \hat{e} \, d\Omega + \int_{\Omega^+} \tilde{w}_e \tilde{e} \, d\Omega + c \int_{\Omega^+} \mathbf{V}\tilde{w}_e \cdot \mathbf{V}\hat{e} \, d\Omega + c \int_{\Omega^+} \mathbf{V}\tilde{w}_e \cdot \mathbf{V}\tilde{e} \, d\Omega = \int_{\Omega^+} \tilde{w}_e \varepsilon_{eq} \, d\Omega \quad \forall \tilde{w}_e \in H^1(\Omega). \tag{32b}$$

5. Discretisation and linearisation of the governing equations

In this section the linearised form of the governing equations for a body crossed by a discontinuity is developed. In the following, the subscript h will be dropped from discretised quantities. Engineering notation for $\boldsymbol{\sigma}$ and $\boldsymbol{\varepsilon}$ is used.

5.1. Problem field description

Using a Bubnov–Galerkin approach, Eqs. (1)–(3) can be discretised in each element 'affected' by the enhancement using

$$\hat{\mathbf{u}} = \mathbf{N}_u \mathbf{a}, \quad \tilde{\mathbf{u}} = \mathbf{N}_u \mathbf{b}, \quad \mathbf{V}^s \hat{\mathbf{u}} = \mathbf{B}_u \mathbf{a}, \quad \mathbf{V}^s \tilde{\mathbf{u}} = \mathbf{B}_u \mathbf{b}, \tag{33}$$

$$\hat{\mathbf{w}}_u = \mathbf{N}_u \mathbf{a}', \quad \tilde{\mathbf{w}}_u = \mathbf{N}_u \mathbf{b}', \quad \mathbf{V}^s \hat{\mathbf{w}}_u = \mathbf{B}_u \mathbf{a}', \quad \mathbf{V}^s \tilde{\mathbf{w}}_u = \mathbf{B}_u \mathbf{b}' \tag{34}$$

for the displacement field, and using

$$\hat{e} = \mathbf{N}_e \mathbf{p}, \quad \tilde{e} = \mathbf{N}_e \mathbf{q}, \quad \mathbf{V}\hat{e} = \mathbf{B}_e \mathbf{p}, \quad \mathbf{V}\tilde{e} = \mathbf{B}_e \mathbf{q}, \tag{35}$$

$$\hat{w}_e = \mathbf{N}_e \mathbf{p}', \quad \tilde{w}_e = \mathbf{N}_e \mathbf{q}', \quad \mathbf{V}\hat{w}_e = \mathbf{B}_e \mathbf{p}', \quad \mathbf{V}\tilde{w}_e = \mathbf{B}_e \mathbf{q}' \tag{36}$$

for the non-local equivalent strain field. In the above relations, $\mathbf{N}_{u/e}$ is a matrix containing the usual finite-element shape functions, $\mathbf{B}_{u/e}$ is a matrix containing spatial derivatives of the shape functions, $\mathbf{a}$ and $\mathbf{b}$ are regular and extra displacement degrees of freedom, and $\mathbf{p}$ and $\mathbf{q}$ are regular and extra non-local equivalent strain degrees of freedom; the primes refer to admissible variations. For elements not affected by the enhancement, the problem fields can be discretised in a standard fashion, considering only standard displacement degrees of freedom $\mathbf{a}$ and non-local equivalent strain degrees of freedom $\mathbf{p}$.

5.2. Discretised and linearised weak equations

The discrete format of the problem fields leads to two discrete weak governing equations for the displacement part in Eq. (25):

$$\int_{\Omega} \mathbf{B}_u^{\mathrm{T}} \boldsymbol{\sigma} \, \mathrm{d}\Omega = \int_{\Gamma_t} \mathbf{N}_u^{\mathrm{T}} \bar{\mathbf{t}} \, \mathrm{d}\Gamma, \tag{37a}$$

$$\int_{\Omega^+} \mathbf{B}_u^{\mathrm{T}} \boldsymbol{\sigma} \, \mathrm{d}\Omega = \int_{\Gamma_t^+} \mathbf{N}_u^{\mathrm{T}} \bar{\mathbf{t}} \, \mathrm{d}\Gamma, \tag{37b}$$

from which the equivalent nodal force vector related to admissible variations of **a** and **b** result in

$$\mathbf{f}_{\mathrm{int},a} = \int_{\Omega} \mathbf{B}_u^{\mathrm{T}} \boldsymbol{\sigma} \, \mathrm{d}\Omega, \quad \mathbf{f}_{\mathrm{ext},a} = \int_{\Gamma_t} \mathbf{N}_u^{\mathrm{T}} \bar{\mathbf{t}} \, \mathrm{d}\Gamma, \tag{38a}$$

$$\mathbf{f}_{\mathrm{int},b} = \int_{\Omega^+} \mathbf{B}_u^{\mathrm{T}} \boldsymbol{\sigma} \, \mathrm{d}\Omega, \quad \mathbf{f}_{\mathrm{ext},b} = \int_{\Gamma_t^+} \mathbf{N}_u^{\mathrm{T}} \bar{\mathbf{t}} \, \mathrm{d}\Gamma. \tag{38b}$$

For the modified Helmholtz equation, substitution of the discretised non-local equivalent strain into Eq. (32), leads to two discrete weak governing equations:

$$\int_{\Omega} \mathbf{N}_e^{\mathrm{T}} \mathbf{N}_e \mathbf{p} \, \mathrm{d}\Omega + \int_{\Omega^+} \mathbf{N}_e^{\mathrm{T}} \mathbf{N}_e \mathbf{q} \, \mathrm{d}\Omega + \int_{\Omega} \mathbf{B}_e^{\mathrm{T}} c \mathbf{B}_e \mathbf{p} \, \mathrm{d}\Omega + \int_{\Omega^+} \mathbf{B}_e^{\mathrm{T}} c \mathbf{B}_e \mathbf{q} \, \mathrm{d}\Omega = \int_{\Omega} \mathbf{N}_e^{\mathrm{T}} \varepsilon_{\mathrm{eq}} \, \mathrm{d}\Omega, \tag{39a}$$

$$\int_{\Omega^+} \mathbf{N}_e^{\mathrm{T}} \mathbf{N}_e \mathbf{p} \, \mathrm{d}\Omega + \int_{\Omega^+} \mathbf{N}_e^{\mathrm{T}} \mathbf{N}_e \mathbf{q} \, \mathrm{d}\Omega + \int_{\Omega^+} \mathbf{B}_e^{\mathrm{T}} c \mathbf{B}_e \mathbf{p} \, \mathrm{d}\Omega + \int_{\Omega^+} \mathbf{B}_e^{\mathrm{T}} c \mathbf{B}_e \mathbf{q} \, \mathrm{d}\Omega = \int_{\Omega^+} \mathbf{N}_e^{\mathrm{T}} \varepsilon_{\mathrm{eq}} \, \mathrm{d}\Omega, \tag{39b}$$

from which the equivalent nodal 'force' vectors related to admissible variations of **p** and **q** result in

$$\mathbf{f}_{\mathrm{int},p} = \int_{\Omega} (\mathbf{N}_e^{\mathrm{T}} \mathbf{N}_e \mathbf{p} + \mathbf{B}_e^{\mathrm{T}} c \mathbf{B}_e \mathbf{p} - \mathbf{N}_e^{\mathrm{T}} \varepsilon_{\mathrm{eq}}) \, \mathrm{d}\Omega + \int_{\Omega^+} (\mathbf{N}_e^{\mathrm{T}} \mathbf{N}_e \mathbf{q} + \mathbf{B}_e^{\mathrm{T}} c \mathbf{B}_e \mathbf{q}) \, \mathrm{d}\Omega, \tag{40a}$$

$$\mathbf{f}_{\mathrm{int},q} = \int_{\Omega^+} (\mathbf{N}_e^{\mathrm{T}} \mathbf{N}_e \mathbf{p} + \mathbf{B}_e^{\mathrm{T}} c \mathbf{B}_e \mathbf{p} - \mathbf{N}_e^{\mathrm{T}} \varepsilon_{\mathrm{eq}}) \, \mathrm{d}\Omega + \int_{\Omega^+} (\mathbf{N}_e^{\mathrm{T}} \mathbf{N}_e \mathbf{q} + \mathbf{B}_e^{\mathrm{T}} c \mathbf{B}_e \mathbf{q}) \, \mathrm{d}\Omega. \tag{40b}$$

The external part of the RHS is empty due to the applied boundary conditions ($\mathbf{f}_{\mathrm{ext},p} = \mathbf{f}_{\mathrm{ext},q} = \mathbf{0}$).

To develop a consistent incremental-iterative full Newton–Raphson procedure, the governing equations are linearised following standard procedures (see e.g. Refs. [6,13]). At iteration i within a time step n, the discretised coupled boundary value problem can be written in matrix format as:

$$\begin{bmatrix} \mathbf{K}_{aa}^{n,i-1} & \mathbf{K}_{ab}^{n,i-1} & \mathbf{K}_{ap}^{n,i-1} & \mathbf{K}_{aq}^{n,i-1} \\ \mathbf{K}_{ba}^{n,i-1} & \mathbf{K}_{bb}^{n,i-1} & \mathbf{K}_{bp}^{n,i-1} & \mathbf{K}_{bq}^{n,i-1} \\ \mathbf{K}_{pa}^{n,i-1} & \mathbf{K}_{pb}^{n,i-1} & \mathbf{K}_{pp}^{n,i-1} & \mathbf{K}_{pq}^{n,i-1} \\ \mathbf{K}_{qa}^{n,i-1} & \mathbf{K}_{qb}^{n,i-1} & \mathbf{K}_{qp}^{n,i-1} & \mathbf{K}_{qq}^{n,i-1} \end{bmatrix} \begin{bmatrix} \delta \mathbf{a}^{n,i} \\ \delta \mathbf{b}^{n,i} \\ \delta \mathbf{p}^{n,i} \\ \delta \mathbf{q}^{n,i} \end{bmatrix} = \begin{bmatrix} \mathbf{f}_{\mathrm{ext},a}^{n} \\ \mathbf{f}_{\mathrm{ext},b}^{n} \\ \mathbf{0} \\ \mathbf{0} \end{bmatrix} - \begin{bmatrix} \mathbf{f}_{\mathrm{int},a}^{n,i-1} \\ \mathbf{f}_{\mathrm{int},b}^{n,i-1} \\ \mathbf{f}_{\mathrm{int},p}^{n,i-1} \\ \mathbf{f}_{\mathrm{int},q}^{n,i-1} \end{bmatrix} \tag{41}$$

with the symmetries $\mathbf{K}_{ba} = \mathbf{K}_{ab}$, $\mathbf{K}_{bp} = \mathbf{K}_{bq} = \mathbf{K}_{aq}$, $\mathbf{K}_{qa} = \mathbf{K}_{qb} = \mathbf{K}_{pb}$, $\mathbf{K}_{qp} = \mathbf{K}_{qq} = \mathbf{K}_{pq}$, and

$$\mathbf{K}_{aa} = \int_{\Omega} \mathbf{B}_u^{\mathrm{T}} (1 - \omega) \mathbf{D} \mathbf{B}_u \, \mathrm{d}\Omega, \tag{42a}$$

$$\mathbf{K}_{ab} = \int_{\Omega^+} \mathbf{B}_u^{\mathrm{T}} (1-\omega) \mathbf{D} \mathbf{B}_u \, \mathrm{d}\Omega, \tag{42b}$$

$$\mathbf{K}_{ap} = - \int_{\Omega} \mathbf{B}_u^{\mathrm{T}} \left[\frac{\partial \omega}{\partial \kappa} \right] \left[\frac{\partial \kappa}{\partial e} \right] \mathbf{D} \boldsymbol{\varepsilon} \mathbf{N}_e \, \mathrm{d}\Omega, \tag{42c}$$

$$\mathbf{K}_{aq} = - \int_{\Omega^+} \mathbf{B}_u^{\mathrm{T}} \left[\frac{\partial \omega}{\partial \kappa} \right] \left[\frac{\partial \kappa}{\partial e} \right] \mathbf{D} \boldsymbol{\varepsilon} \mathbf{N}_e \, \mathrm{d}\Omega, \tag{42d}$$

$$\mathbf{K}_{bb} = \int_{\Omega^+} \mathbf{B}_u^{\mathrm{T}} (1-\omega) \mathbf{D} \mathbf{B}_u \, \mathrm{d}\Omega, \tag{42e}$$

$$\mathbf{K}_{pa} = - \int_{\Omega} \mathbf{N}_e^{\mathrm{T}} \left[\frac{\partial \varepsilon_{\mathrm{eq}}}{\partial \boldsymbol{\varepsilon}} \right]^{\mathrm{T}} \mathbf{B}_u \, \mathrm{d}\Omega, \tag{42f}$$

$$\mathbf{K}_{pb} = - \int_{\Omega^+} \mathbf{N}_e^{\mathrm{T}} \left[\frac{\partial \varepsilon_{\mathrm{eq}}}{\partial \boldsymbol{\varepsilon}} \right]^{\mathrm{T}} \mathbf{B}_u \, \mathrm{d}\Omega, \tag{42g}$$

$$\mathbf{K}_{pp} = \int_{\Omega} (\mathbf{N}_e^{\mathrm{T}} \mathbf{N}_e + \mathbf{B}_e^{\mathrm{T}} c \mathbf{B}_e) \, \mathrm{d}\Omega, \tag{42h}$$

$$\mathbf{K}_{pq} = \int_{\Omega^+} (\mathbf{N}_e^{\mathrm{T}} \mathbf{N}_e + \mathbf{B}_e^{\mathrm{T}} c \mathbf{B}_e) \, \mathrm{d}\Omega. \tag{42i}$$

As in the standard gradient-enhanced damage formulation, the stiffness matrix is not symmetric. The terms in the RHS of the discretised boundary value problem are defined in Eqs. (38) and (40).

6. Finite-element implementation

The finite-element implementation for the continuum response mainly follows the one proposed in Ref. [25] for the gradient-enhanced model. The proposed model has been implemented with linear and quadratic quadrilateral elements. In the following, some issues pertinent to the current implementation of the discontinuous model are discussed. Other issues, such as the choice of the nodes to enhance, are discussed in Refs. [19,32].

6.1. Introducing a discontinuity

In a damaging continuum a critical situation can be defined as one which corresponds to damage values close, or equal, to 1 in the element ahead of a discontinuity tip. The introduction of a discontinuity at (almost) total loss of load-carrying capacity is in line with the narrowing of the strain profile as a consequence of strain localisation (see Fig. 4). Introducing a discontinuity before complete localisation, e.g. when damage is around 90%, poses the problem of defining the correct energy dissipation for the regularised continuous–discontinuous model which is problematic, even in a one-dimensional setting.

As soon a critical situation is detected in the element ahead of a discontinuity tip (i.e. when damage is close to, but less than unity), the traction-free discontinuity is extended. To preserve the robustness of the Newton–Raphson solution procedure, a discontinuity is introduced as a straight segment at the end of a load increment in the element ahead of a discontinuity tip if the initiation criterion is fulfilled. This procedure is
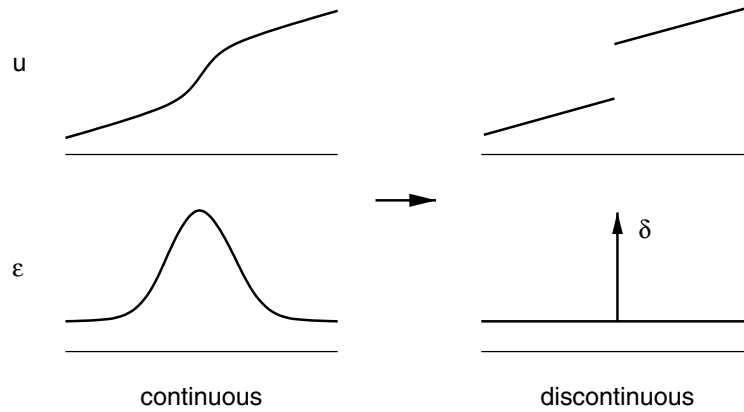
Fig. 4. From continuous to discontinuous displacement/strain profiles as a consequence of strain localisation.

repeated in the elements ahead of this element with the extended discontinuity until the initiation criterion is no longer satisfied. In the applications in Sections 7.1 and 7.2, a traction-free discontinuity is inserted into an element when the damage at all its integration points is larger than a critical value ω_{crit}. The insertion of a discontinuity with damage larger than ω_{crit} at one integration point is considered in Section 7.3. Simulations performed with both criteria (one integration point versus all integration points larger than ω_{crit}) on the same test gave identical results upon mesh refinement.

To reproduce a crack tip, the displacement jump at the discontinuity tip is set to zero. This is achieved by considering only standard **a** and **p** dofs for the nodes on an element boundary touched by a discontinuity (see Ref. [32]). When the discontinuity is extended in the next element, nodes behind the discontinuity tip are enhanced.

6.2. Orienting a discontinuity

In a regularised continuum, the direction of a discontinuity cannot be analytically derived from a bifurcation analysis and phenomenologically based criteria must be used. In this context, since criteria based on the stress tensor cannot be reliably used [32], the direction of maximum accumulation of the non-local equivalent strain in a V-shaped window ahead of a discontinuity tip is used (the V-shaped window spans a circular sector of 90°, see Fig. 5). This criterion can be justified by the observation of numerically computed non-local equivalent strain profiles. The vector in the direction of the discontinuity propagation is computed as [33]:
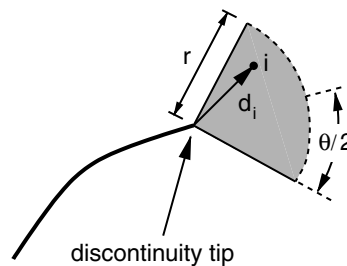
Fig. 5. Determination of the propagation direction.

$$\mathbf{d}_{\Gamma_{\mathrm{d}}} = \sum_{i \in S} e_i V_i w_i \frac{\mathbf{d}_i}{\|\mathbf{d}_i\|}, \tag{43}$$

where S is the set of integration points i in the V-shaped window ahead of a discontinuity tip, e_i is the non-local equivalent strain at integration point i, V_i and w_i are the volume and the weight associated with integration point i, respectively, and $\mathbf{d}_i$ is the vector in the direction of the integration point i. The weights w_i are computed from

$$w_i = \frac{1}{(2\pi)^{3/2} r^3} \exp\left(-\frac{\|\mathbf{d}_i\|^2}{2r^2} \right) \tag{44}$$

with interaction radius r equal to four times the length scale of the gradient-enhanced damage model.

6.3. Numerical integration

When dealing with integration of the element matrices only on part of an element domain, it is necessary to consider alternative integration rules. When an element is intersected by a discontinuity, the two resulting domains are triangulated and each triangular sub-domain is mapped to a parent unit triangle over which a three-point symmetric quadrature rule, with interior points within the triangular sub-domain, is considered [19]. For elements not crossed by a discontinuity, a standard 2×2 Gauss integration scheme is used for numerical convenience.

It is worth noting that the resulting composite integration scheme, which consists of 24 integration points in eight triangular sub-domains, integrates correctly a quadratic function over a parent quadrilateral element. In the numerical integration of the element matrices, this composite integration scheme results, for the terms containing the strain energy density, in a full integration rule for bilinear quadrilateral elements and in a reduced integration rule for a quadratic quadrilateral elements. The actual construction of the composite integration rule is based on an exact algebraic inverse iso-parametric mapping for bilinear quadrilateral elements [35]. This technique is based on the use of quadrilateral elements with straight sides and evenly spaced side nodes.

6.4. Transfer of history data

The transfer of history data within an element is performed after the introduction of a discontinuity in an element. Since smoothing techniques [33] would result in smaller values for the maximum value κ of the non-local equivalent strain e driving damage evolution, violating thus the Kuhn–Tucker conditions in Eq. (11), the maximum value of κ within the element is considered as representative of the state of the entire element. The error introduced diminishes upon mesh refinement. After the transfer is performed, the increment which led to the critical damage value is recomputed to allow a consistent damage growth in the elements around the discontinuity tip.

7. Numerical simulations

In this section, the combined continuous–discontinuous approach to failure is applied to quasi-brittle failure in concrete and composite specimens. A full Newton–Raphson procedure has been used to trace the response in the non-linear regime. Although the algorithm was consistently derived to obtain quadratic convergence, the performance of the model close to failure and before the extension a discontinuity in a

critically damaged area deteriorated (as $\omega \to 1$). However, after the extension of a discontinuity, quadratic convergence was retrieved.

7.1. Concrete beam in four-point bending

A four-point bending test of a concrete beam with different notch sizes d is analysed (see Fig. 6). To enable comparison with the experiments [10], the vertical displacement of a point placed at the bottom of the beam and with an offset of 7.5 mm from the centreline of the beam is used for the measurement of the deflection v. The following model parameters, 'fitted' for the continuous problem, are adopted for the simulation [21]: Young's modulus $E = 40\,000$ MPa; Poisson's ratio $v = 0.2$; exponential damage evolution law (see Eq. (12)) with $\kappa_0 = 0.000075$, $\alpha = 0.92$ and $\beta = 300$; modified von Mises definition of the local equivalent strain (see Eq. (16)) with $k = 10$ and gradient parameter $c = 4$ mm^2. The simulation is performed under plane stress conditions. The load is applied via an imposed displacement and quadrilateral elements with quadratic interpolation for the displacement and bilinear interpolation for the non-local equivalent strain have been used. The notch is simulated as a traction-free discontinuity. The traction-free discontinuity is extended, starting from the tip at the notch, when the damage at all integration points in the
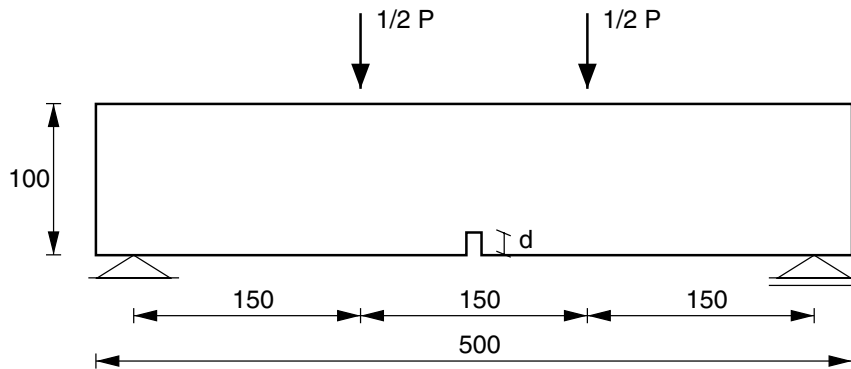
Fig. 6. Geometry and boundary conditions for the four-point bending test (thickness = 50 mm; all dimensions in mm).
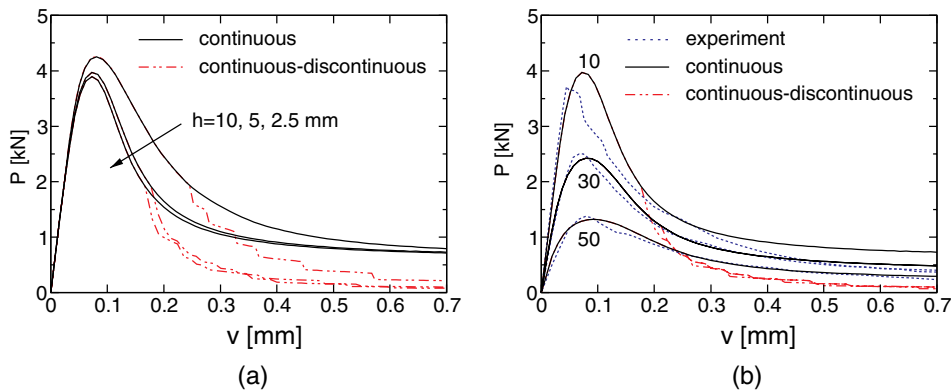
Fig. 7. Load–deflection curves for simulations with (a) different meshes for a 10 mm deep notch (h is the element size in the central part of the beam) and (b) different notch size d for the medium element size mesh ($h = 5$ mm) and experimental results [10].
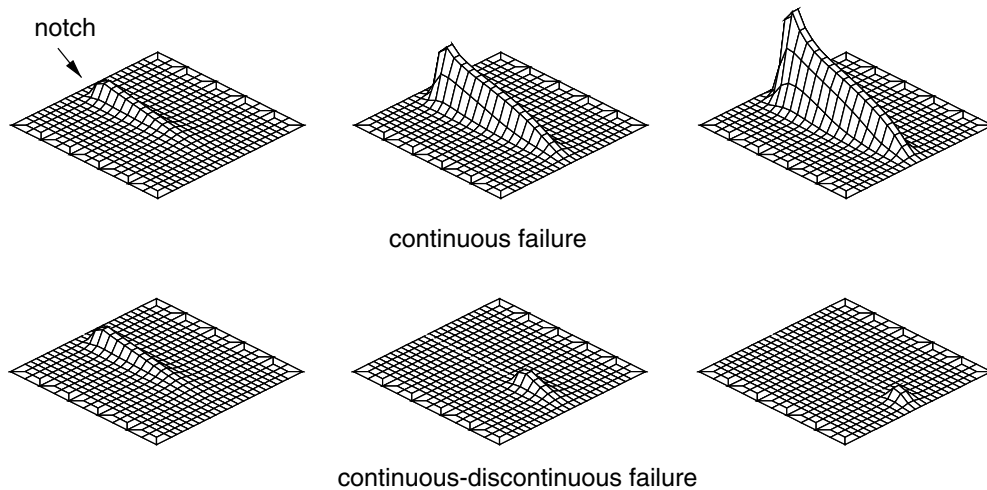
Fig. 8. Four-point bending test: non-local equivalent strain evolution (plotted in the same scale for the 10 mm deep notch beam with medium element size mesh; close-up of the central part of the beam).
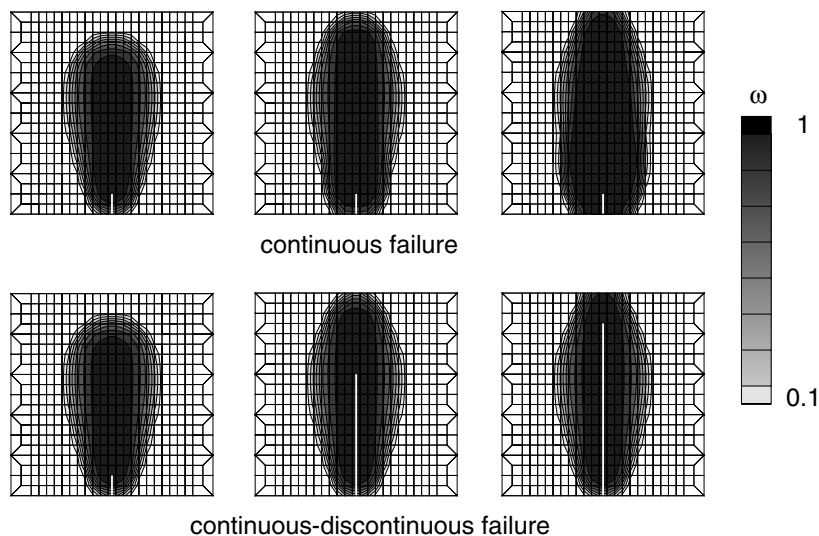

Fig. 9. Four-point bending test: damage evolution (the discontinuity is represented by the white thick line; 10 mm deep notch beam with medium element size mesh; close-up of the central part of the beam).

element ahead of the discontinuity tip is larger than a critical value, set to $\omega_{\text{crit}} = 0.999$; the discontinuity is prescribed to be vertical.

The analyses for the 10 mm deep notch beam are reported in Fig. 7a for different meshes. In the central part of the mesh, the coarse, medium and fine mesh element size h is 10, 5 and 2.5 mm, respectively. Due to the small difference in the response between the medium and the fine discretisation (see Fig. 7a), the former, with a 10 mm deep notch, has been used for the results depicted in Figs. 8 and 9.

From the analysis, it is evident how the introduction of a discontinuity during the computation influences the global (load–displacement curve) and local (damage and non-local equivalent strain profiles) behaviour. In particular, Fig. 8 shows how the activity of the non-local equivalent strain is mobilised only around the discontinuity tip for the continuous–discontinuous model. This translates into the more realistic damage profiles depicted in Fig. 9 where, in contrast to the continuous model alone, the width of the damage zone at the bottom of the specimen does not increase with the combined continuous–discontinuous failure model. However, the use of an exponential softening relationship with a high residual stress at the moment of the enhancement causes the marked drops reported in Fig. 7a and makes the comparison with the experiment, reported in Fig. 7b, difficult (this issue is discussed in Section 7.4). Responses of computations with higher values of ω_{crit} show a better agreement at the global level with experimental results but this is due to the delayed or, in some cases, precluded extension of a discontinuity. The use of different damage law parameters to achieve lower residual stress values produced an unsatisfactory comparison in the post-peak response (note that this consideration relates to the continuous model alone since the discontinuity is extended at a later stage as depicted in Fig. 7). Introduction of displacement discontinuities requires a re-assessment of the continuous model parameters which govern the post-peak response, which has not been done.

7.2. Composite compact–tension specimen

The compact–tension specimen depicted in Fig. 10 [1], experimentally tested in Ref. [8] and numerically analysed in Refs. [4,7,22], has been numerically investigated with the combined continuous–discontinuous model. The specimen is placed on two loading pins whose action has been modelled by applying two vertical forces in the uppermost and lowermost node of the pinholes via deformation control. In the simulations, indirect displacement control has been used, with the displacement (crack mouth opening displacement, cmod) measured between two markers placed 25 mm from the left edge and 14 mm from the
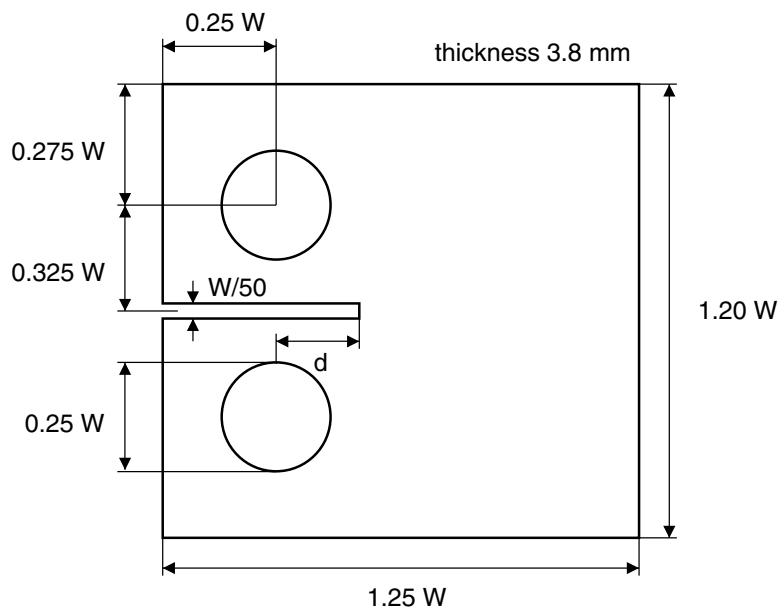

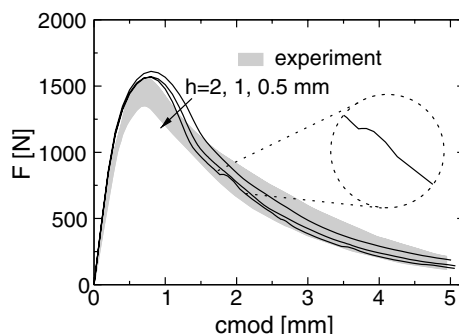Fig. 10. Compact–tension specimen ($W = 50$ mm, $d = 10$ mm).

Fig. 11. Load–cmod diagrams for the compact–tension specimen for different mesh resolutions (h indicates the average element size in the central part of the specimen).

symmetry axis of the specimen [4]; the vertical displacement of the mid-side point on the right central part of the specimen has been restrained, as well as the horizontal displacement of the right lowermost and uppermost corners. A small part of the notch is simulated as a traction-free discontinuity. The discontinuity is extended when the damage at all integration points in the element ahead of the discontinuity tip is larger than $\omega_{\mathrm{crit}} = 0.99995$ and its direction is computed according to the direction of maximum non-local equivalent strain as described in Section 6.2. The simulations are performed using unstructured meshes of bilinear quadrilateral elements under plane stress conditions with average element sizes h in the central part of the specimen equal to 2, 1, 0.5 mm with 443, 1209 and 3955 elements, respectively. The model parameters have been adopted from Geers et al. [7]: damage growth is expressed via the power law in Eq. (13) with $\kappa_0 = 0.011$, $\kappa_{\mathrm{c}} = 0.5$, $\alpha = 5$ and $\beta = 0.75$; the equivalent strain definition is based on the positive principal strain components (see Eq. (17)); Young's modulus $E = 3200$ MPa; Poisson's ratio $v = 0.28$ and gradient parameter $c = 2$ mm^2. To avoid damage growth in the elements around the pinholes, a higher value of κ_0 has been given to elements in these areas. Furthermore, an almost horizontal branch was added to the softening law at $\kappa = 0.385\kappa_{\mathrm{c}}$, which corresponds, in an ideal one-dimensional uniform tension test, to an almost nil residual stress ($0.175\%\kappa_0 E$) (see Section 7.5).

The load–cmod response is shown in Fig. 11. The agreement between the experimental response and the results of the simulations is excellent. However, the response computed with the finer mesh ($h = 0.5$ mm) shows bumps after the extension of the discontinuity (this issue is discussed in detail in Section 7.5). The evolution of the fracture process is shown in Fig. 12 for the simulation related to the finest of the meshes used ($h = 0.5$ mm). For a comparison, the local and global response of the standard model (no propagating discontinuity) and of the combined continuous–discontinuous model are shown in Figs. 13 and 14, respectively. Although the differences in the global response are not significant (see Fig. 14), the combined model provides a better representation of the failure process (compare Fig. 12 with Fig. 13).

7.3. Single-edge notched beam in anti-symmetric four-point-shear loading

A single-edge notched beam, depicted in Fig. 15, is subjected to an anti-symmetric four-point-shear loading [27]. Fig. 15 shows the applied boundary conditions which result in a curved crack path, from the lower-right part of the notch towards a point to the right of the lower-right support as depicted in Fig. 16.

The supports have widths of 20 mm with the centre located 20 mm out of the mid-span of the beam.

The beam is analysed in a plane stress situation with bilinear quadrilateral elements; the simulations are performed using unstructured meshes with average element size h in the central part of beam equal to 4, 2 and 1 mm with 674, 2148 and 7308 elements, respectively. The model parameters are adopted unaltered
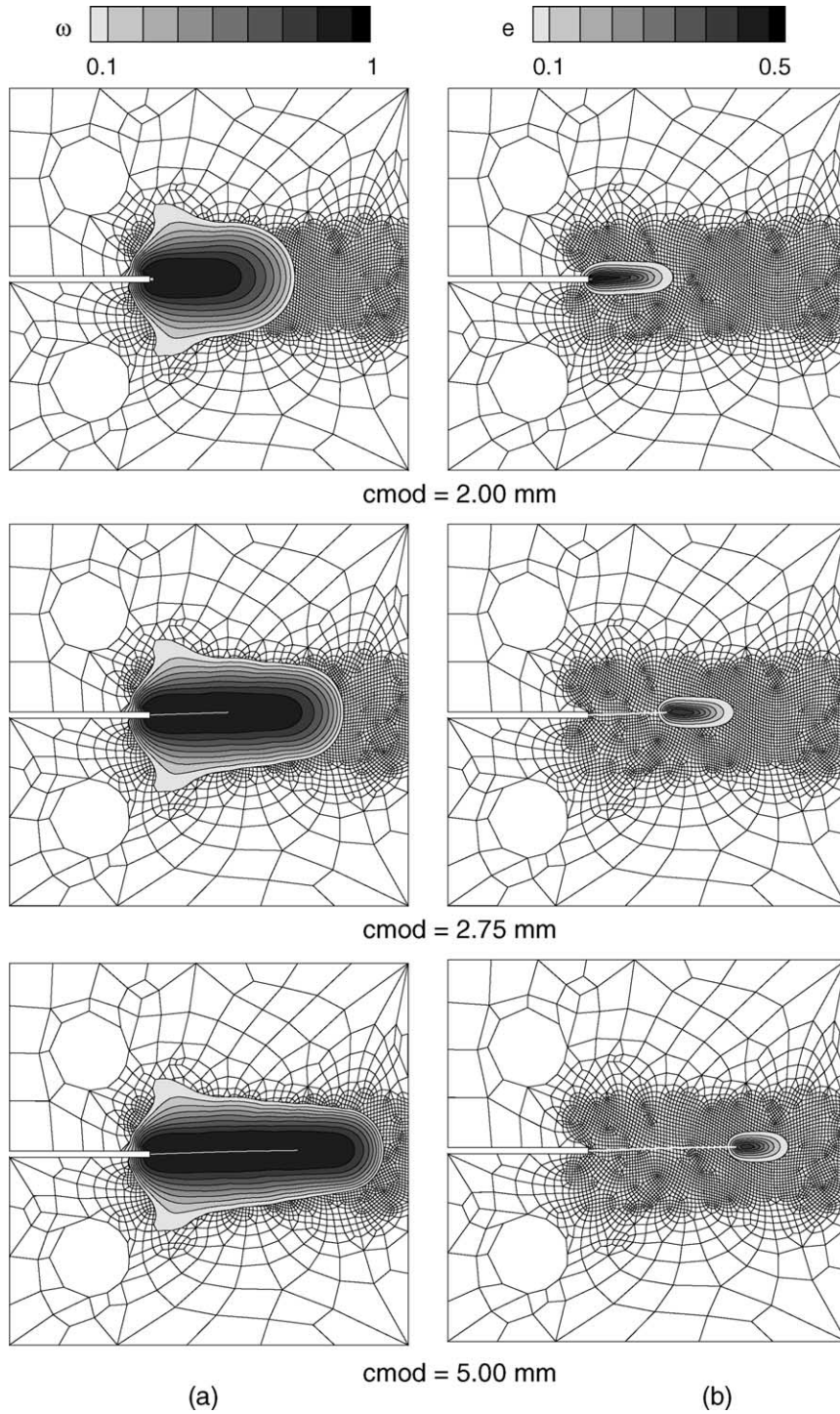
Fig. 12. Evolution of the failure process: (a) damage ω and (b) non-local equivalent strain e contour plots.
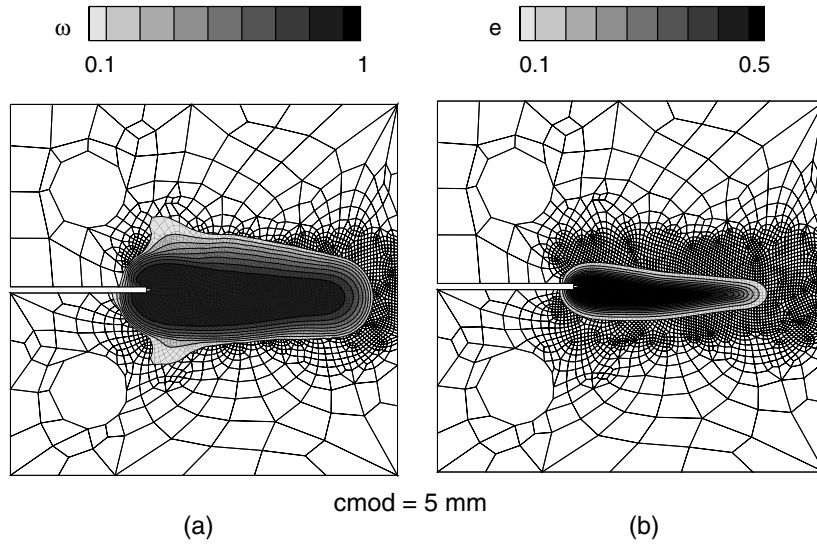
Fig. 13. Final failure state with the continuous model (no propagating discontinuity): (a) damage ω and (b) non-local equivalent strain e contour plots.
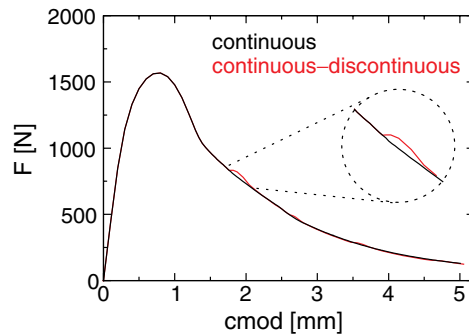

Fig. 14. Load–cmod diagrams for the compact–tension specimen ($h = 0.5$ mm): comparison between continuous and continuous–discontinuous model.
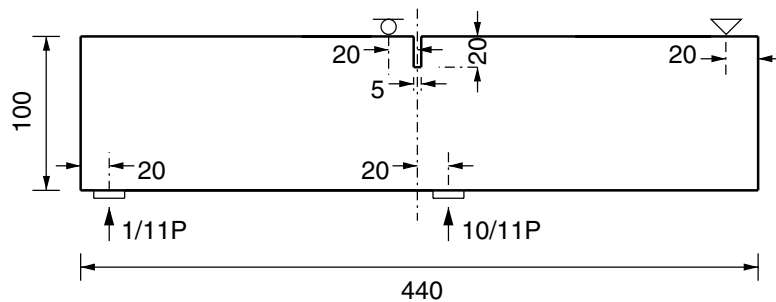
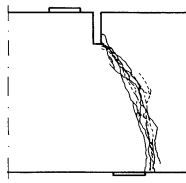

Fig. 15. Single-edge notched beam [27] (depth = 100 mm; all dimensions in mm).

Fig. 16. Experimental crack patterns from three single-edge notched beams (adapted from Schlangen [27]).
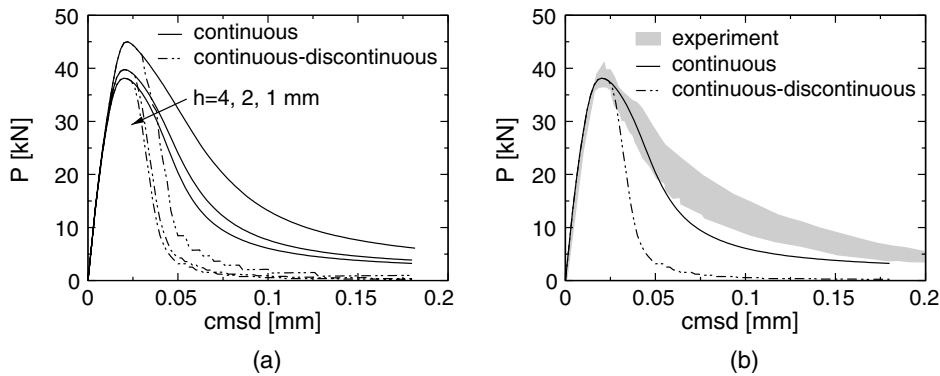
Fig. 17. Applied load against cmsd: (a) convergence studies and (b) comparison with the experimental response [27] for the $h = 1$ mm mesh (h indicates the average element size in the central part of the beam).

from Peerlings et al. [23] who performed analyses in a purely continuous setting: Young's modulus $E = 35\,000$ MPa, Poisson's ratio $v = 0.2$, gradient parameter $c = 1$ mm^2, modified von Mises equivalent strain definition in Eq. (16) with $k = 10$, exponential softening law in Eq. (12) with $\kappa_0 = 0.00006$, $\alpha = 0.96$ and $\beta = 100$. The loading platens have a Young's modulus one order of magnitude larger than the concrete.

The load is applied by means of an indirect displacement control procedure with the crack mouth sliding displacement (cmsd), defined as the relative vertical displacement of the opposite faces of the notch, taken as control parameter [22]. The traction-free discontinuity is extended when damage is larger that $\omega_{\text{crit}} = 0.99$ at one integration point in the element ahead of the discontinuity tip. It starts from an initial horizontal traction-free discontinuity (the horizontal traction-free discontinuity goes from (222.5; 80.1) to (223; 80.1), with the origin of the coordinate system placed at the lowermost left corner of the beam). As in the previous example, the direction of the discontinuity is aligned with the direction of the maximum accumulation of non-local equivalent strain.

Similar to the case of the four-point bending test reported in Section 7.1, the global response of the continuous–discontinuous model, reported in Fig. 17 in terms of load–cmsd, is more brittle than that of the continuous model. This makes the comparison with the experiment difficult (see Fig. 17b). This issue is discussed in the next section. However, it is worth noting that the convergence of the iterative scheme for the continuous–discontinuous approach is faster (see Fig. 17a). The final failure pattern is reported in Figs. 18–20 together with a comparison of failure patterns for the continuous and the continuous–discontinuous model. In particular, Fig. 18 shows that the evolution of damage is in good agreement with the observed crack pattern reported in Fig. 16 and that the direction of the discontinuity is correctly determined even with the coarsest of the discretisations (see Fig. 18a). A close-up of the final damage distribution and traction-free discontinuity for the $h = 1$ mm mesh is shown in Fig. 19, and the continuous–discontinuous
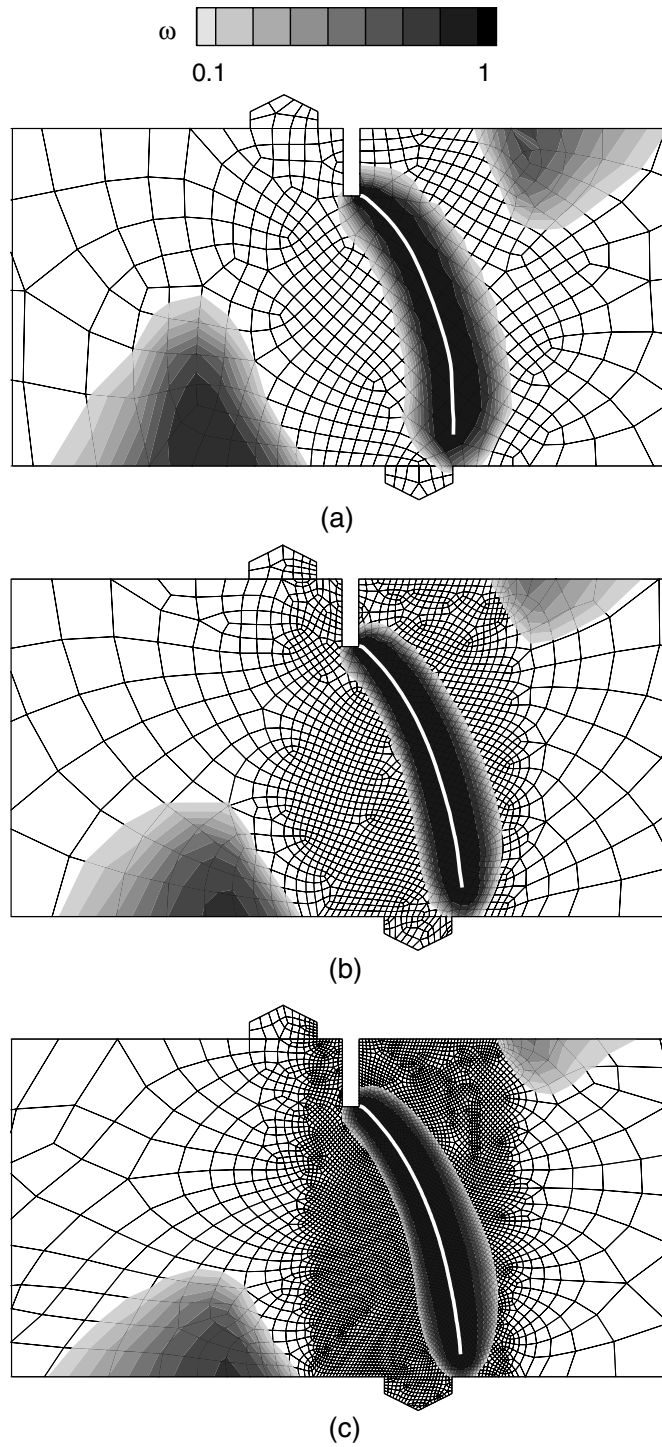
Fig. 18. Final damage distribution and traction-free discontinuity for the (a) $h = 4$ mm, (b) $h = 2$ mm and (c) $h = 1$ mm meshes (close-up of the central part of the beam).
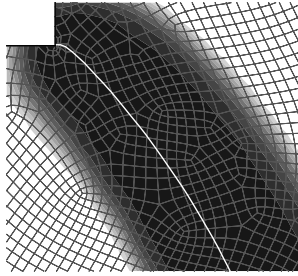
Fig. 19. Close-up of the final damage distribution and traction-free discontinuity for the $h = 1$ mm mesh near the notch.
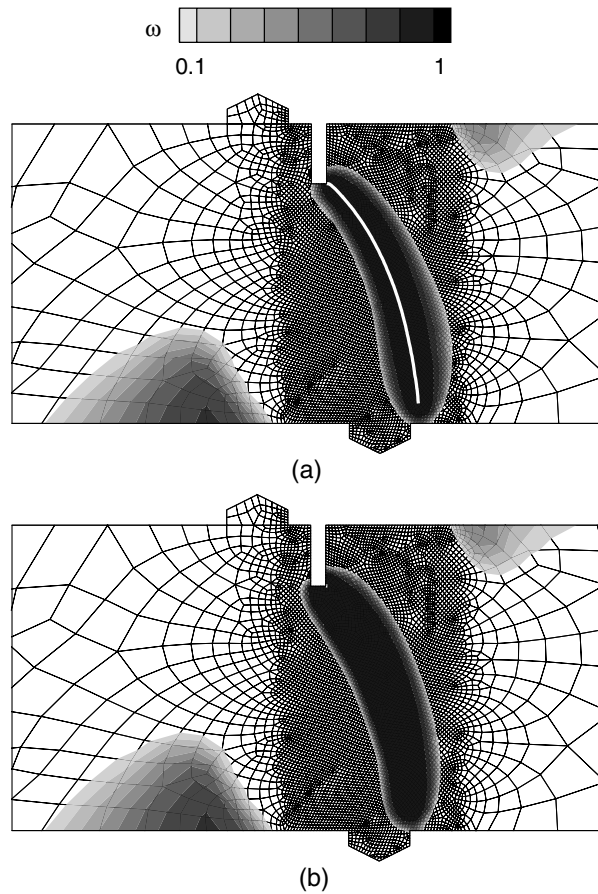

Fig. 20. Final failure characterisation for (a) the continuous–discontinuous model and (b) the continuous model (no propagating discontinuity) for the $h = 1$ mm mesh (close-up of the central part of the beam).

model and the continuous model are contrasted in Fig. 20 where it is clear that the introduction of the discontinuity avoids the unrealistic damage growth close to the notch (see Fig. 20a).
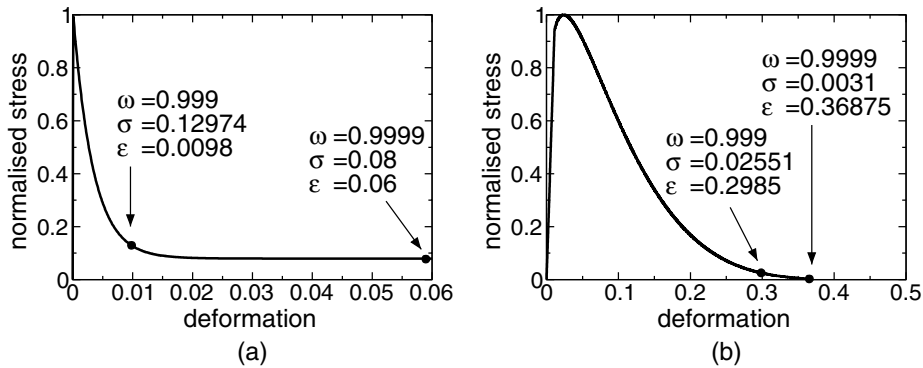
Fig. 21. Stress–strain-softening curves for exponential (a) and power (b) law of damage growth.

7.4. Stress–strain relationships

Enhancing an element with a discontinuous interpolation of the problem fields when the damage in all its integration points is larger than $\omega_{crit} = 0.999$ or larger than $\omega_{crit} = 0.9999$ may result in significant differences in terms of the global response. To understand the differences originating from the choice of stress–strain relationships, the normalised stress–strain-softening paths for a one-dimensional uniform loading state field are contrasted. The model parameters of the four-point bending test and the compact–tension test previously analysed are adopted. The results of this analysis are shown in Fig. 21.

For the exponential law in Eq. (12) (see Fig. 21a), an increment of less than 1% in damage requires an increment of approximately 512% in deformation which corresponds to a drop in the normalised stress of about 39%; for the power law in Eq. (13) (see Fig. 21b), only an increase of 23% in the deformation is necessary to drop the stress of about 88% for the same increment of damage.

The drops in the global response reported in Figs. 7 and 17 are due to an incorrect energy dissipation related to the high residual stress at the moment of the enhancement of the displacement field—despite high damage ($\omega \cong 1$), high stresses can still develop. Although the asymptote of the exponential softening curve in Fig. 21a might be useful in reproducing the long tail observed in load–displacement diagrams of concrete specimens which is related to crack bridging [10,17], the physical relevance of these laws is questionable since an analogous and more pronounced phenomenon occurs in fibre-reinforced composite polymers where softening laws with full stress relaxation at finite strain—or laws with a small residual stress—suffice. In light of the combined continuous–discontinuous model, parameters of softening laws should be regarded as model-related parameters rather than material-related parameters.

7.5. Damage initiation and discontinuities

A different phenomenon can be observed in the global response of the compact–tension test depicted in Fig. 11. In the simulations of the compact–tension test with the finest of the meshes, the load–displacement curve showed a bump after the extension of a discontinuity. To better understand the cause of this problem, it is important to realise that, as a result of non-local averaging, the non-local equivalent strain differs quantitatively and qualitatively from its local counterpart. With a strongly concave boundary, as in the case of a sharp notch, non-local regularisation results in a finite value of the damage driving quantity at the crack tip, unlike in the case of the standard continuum where the equivalent strain mimics the singularity of the strain field. However, in contrast to a standard continuum, the maximum of the damage driving

quantity is not located at the tip, but shifted away from it. Simple analytical considerations show that, for a planar crack, the position of the maximum of the non-local equivalent strain is a function of the length scale (i.e. the maximum of the non-local equivalent strain is at the crack tip for a length scale equal to zero). As a consequence, damage reaches its maximum inside the specimen, away from the tip. Note that although the condition for the propagation of a discontinuity might be satisfied in the specimen, it is *not* necessarily at the crack tip. Eventually, due to increasing loading, the portion of the specimen where damage has its maximum enlarges and reaches the crack tip, thus allowing for the propagation of the discontinuity. Further, for computational reasons, since damage can reach values larger than ω_{crit} away from the discontinuity tip, the use of exponential-like softening laws (or any other law with full stress relaxation at infinite strain) is necessary to avoid singularity in the global stiffness matrix.

The discontinuity propagates through more that one element at a time and, as a consequence, is accompanied by strong variations of the local equivalent strain which in turn affect its non-local counterpart. It is shown later that this influence is proportional to the length scale. This affects the loading condition at points ahead of the new discontinuity tip which now experience unloading and, due to an increased loading level, generates a structural pseudo-elastic loading, resulting in an incorrect global response.
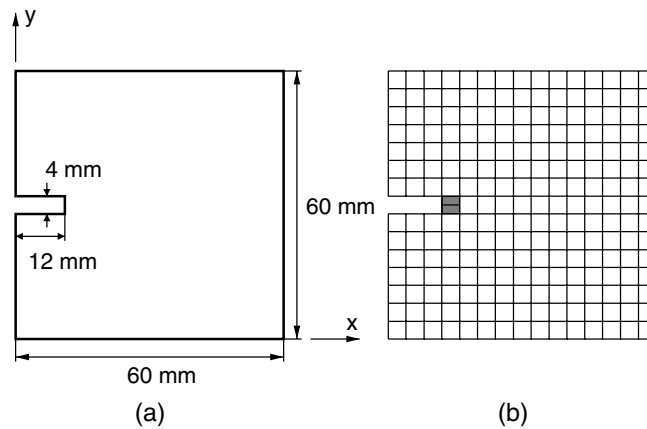

Fig. 22. Compact–tension test: (a) geometry (thickness = 1 mm) and (b) mesh (traction-free discontinuity in the shaded element from $x = 12$ to 16 mm at $y = 0$ mm).
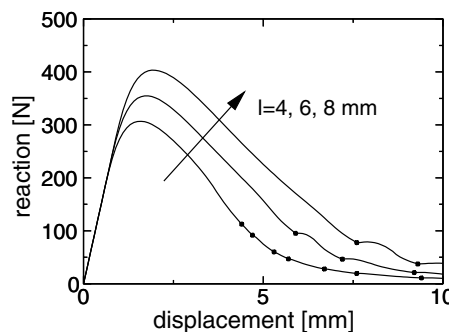

Fig. 23. Load–displacement curves for increasing non-locality parameter l (the dots represent the extension of the discontinuity).
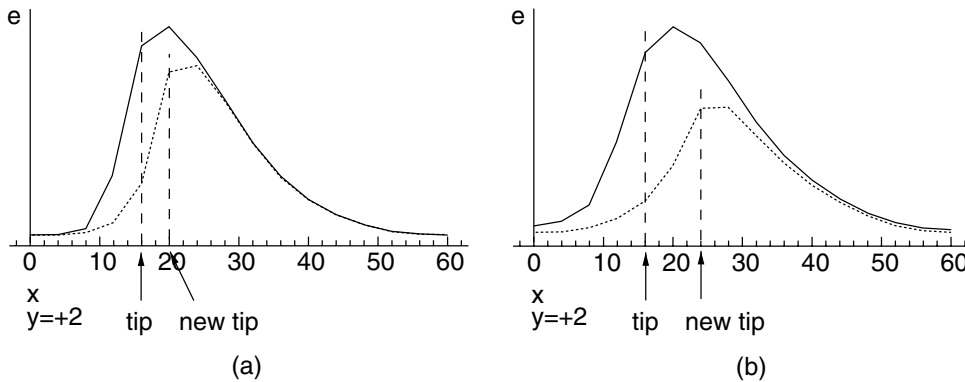
Fig. 24. Non-local equivalent strain profile before (—) and after ($\cdots$) the extension of the discontinuity for (a) $l = 4$ mm and (b) $l = 8$ mm (not to scale).

7.5.1. Numerical considerations

To gain more insight into the nature of the problem, a simpler compact–tension test geometry, depicted in Fig. 22a, has been considered. To reproduce the effect of the discretisation on non-local averaging, different values of c have been used, keeping the mesh unchanged (structured mesh with 4 mm $\times$ 4 mm linear quadrilateral elements; element size $e_{\text{size}} = 4 \times \sqrt{2}$ mm; see Fig. 22b). The load is applied at the uppermost and lowermost left corners ($x = 0$ mm, $y = 0$ mm/$y = 60$ mm) via an applied displacement. The uppermost and lowermost right corners are restrained in the horizontal direction while the nodes at $x = 60$ mm, $y = \pm 2$ mm are restrained in the vertical direction. To avoid damage where the load is applied, a higher value of κ_0 (see Eq. (13)) has been given to the material in the area around the uppermost and lowermost left corners. The model parameters used in the previous simulation of the compact–tension test (see Section 7.2) with $v = 0$ and $\beta = 1$ have been considered. A horizontal traction-free discontinuity is placed in the shaded element depicted in Fig. 22b. The traction-free discontinuity is extended horizontally in the neighbouring element(s) if in all its(their) integration points damage is larger than $\omega_{\text{crit}} = 0.99999$.

The influence of the non-local averaging is illustrated in Fig. 23, where load–displacement curves related to the vertical uppermost restrained node for different values of the length scale have been plotted. The values used for c are 8, 18 and 32 mm^2 which correspond to a length scale l equal to 4, 6 and 8 mm. Compared to the element size e_{size}, only the last one permits sufficient non-local interaction. However, no estimate of the necessary/sufficient number of elements in the process zone is available for differential non-local models and the ratio e_{size}/l is often taken very close to 1 and sometimes even larger. From the curves in Fig. 23 it is evident how an increasing non-local interaction leads to bumps in the load–displacement response after the extension of the discontinuity (the extension is marked by the dots).

The bumps in Fig. 23 originate from the loading situation after the extension of the discontinuity in the elements ahead of the discontinuity tip. This phenomenon can be understood as the combination of two effects: (i) the sudden extension of the discontinuity through several elements due to the shift of the maximum of the non-local equivalent strain away from the crack tip and (ii) the influence of non-local interaction on the unloading of points adjacent to the discontinuity, with the influence proportional to the degree of non-local interaction.

The non-local equivalent strain profiles depicted in Fig. 24, for different degrees of non-local interaction before and after the first extension of the discontinuity, illustrate the problem with the loading condition discussed above. Due to the definition of the loading function (see Eq. (11)), when non-local interaction is strong (Fig. 24b) all the integration points ahead of the discontinuity tip will temporarily unload after its extension. Despite the high damage value in these integration points, they contribute to the RHS through
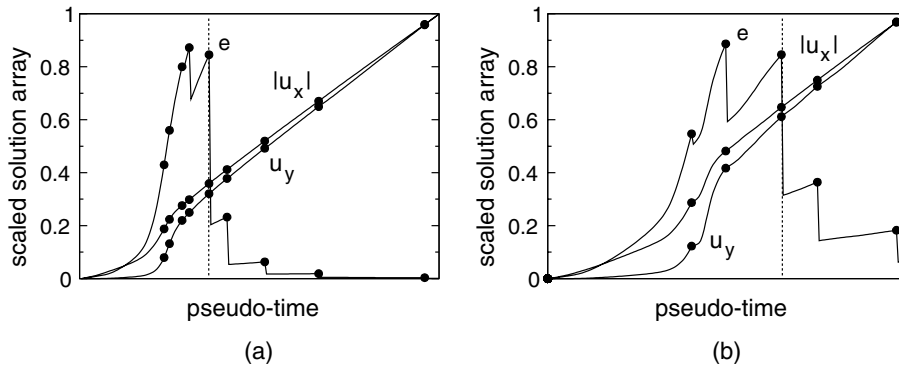
Fig. 25. Evolution of **u** and e for a point located at $x = 32$ mm, $y = 2$ mm for (a) $l = 4$ mm and (b) $l = 8$ mm (the dots represent the extension of the discontinuity and the dotted line indicates the first moment at which the point is behind the discontinuity tip).

residual stresses resulting in spurious loading at the global level. If the non-local interaction is weak (Fig. 24a), the difference in the profiles of the non-local equivalent strain ahead of the discontinuity tip is small. The integration points between the new discontinuity tip and the point where the non-local equivalent strain exhibits its maximum value will unload and, since the unloading is limited, there is no evidence at the global level.

The influence of the length scale on the evolution of the solution array (**u** and e) is depicted in Fig. 25. The extension of the discontinuity, marked by the dots, is accompanied by strong variations of the non-local equivalent strain field. Note that this phenomenon is related to the resolution of the mesh with respect to the length scale as depicted in Fig. 25: if a coarse mesh is used it is likely that bumps in the load–displacement response will not appear (see Fig. 7). It is also stressed that the use of cohesive discontinuities do not solve nor alleviate the problem of the bumps which is only related to the non-local nature of the underlying continuum.

8. Conclusions

A framework for the numerical failure analysis in quasi-brittle materials has been presented. An implicit gradient-enhanced continuum damage model is enriched with a discontinuous interpolations of the problem fields. This allows the realistic description of macroscopic cracks evolving from a microcracked material. As a discontinuity propagates, the non-local equivalent strain increases at the discontinuity tip and ceases behind it. Spurious growth of damage can thus be prevented since the non-local interaction between opposite sides of the discontinuity is avoided. Numerical simulations illustrate the performance of the continuous–discontinuous gradient-enhanced damage model in preventing the spurious response normally observed prior to complete failure with the continuous model alone. Although the model successfully eliminates the interaction between fully and partially damaged material locations, some properties of the underlying non-local continuum model for the transition from continuous to combined continuous–discontinuous failure require further research.

References

[1] ASTM, Metals Test Methods and Analytical Procedures, Designation: E 399-90; E 647-99, in: Annual Book of ASTM Standards, vol. 03.01, American Society for Testing and Materials, West Conshohocken, Pennsylvania, 2000.

[2] Z.P. Bažant, T. Belytschko, T.-P. Chang, Continuum model for strain softening, J. Engrg. Mech. 110 (1984) 1666–1692.

[3] T. Belytschko, Z.P. Bažant, Y.-W. Hyun, T.-P. Chang, Strain softening materials and finite-element solutions, Comput. Struct. 23 (1986) 163–180.

[4] R. de Borst, J. Pamin, M.G.D. Geers, On coupled gradient-dependent plasticity and damage theories with a view to localization analysis, Eur. J. Mech. A/Solids 18 (6) (1999) 939–962.

[5] C.A.M. Duarte, J.T. Oden, H-p clouds—an h-p meshless method, Numer. Methods Partial Different. Equat. 12 (6) (1996) 673–705.

[6] M.G.D. Geers, R. de Borst, W.A.M. Brekelmans, R.H.J. Peerlings, Strain-based transient–gradient damage model for failure analyses, Comput. Methods Appl. Mech. Engrg. 160 (1998) 133–153.

[7] M.G.D. Geers, R. de Borst, W.A.M. Brekelmans, R.H.J. Peerlings, Validation and internal length scale determination for a gradient damage model: application to short glass–fibre-reinforced polypropylene, Int. J. Solids Struct. 36 (1999) 2557–2583.

[8] M.G.D. Geers, T. Peijs, W.A.M. Brekelmans, R. de Borst, Experimental monitoring of strain localization and failure behaviour of composite materials, Compos. Sci. Technol. 56 (1996) 1283–1290.

[9] A. Hillerborg, M. Modéer, P.E. Petersson, Analysis of crack formation and crack growth in concrete by means of fracture mechanics and finite elements, Cem. Concr. Res. 6 (6) (1976) 773–782.

[10] D.A. Hordijk, Local approach to fatigue of concrete, Ph.D. Thesis, Delft University of Technology, 1991. Also published asTensile and tensile fatigue behaviour of concrete: experiments, modelling and analyses, HERON 37 (1) (1992) 3–79.

[11] A.R. Ingraffea, Case studies of simulation of fracture in concrete dams, Engrg. Fract. Mech. 35 (1990) 553–564.

[12] J. Janson, J. Hult, Fracture mechanics and damage mechanics—a combined approach, J. Méch. Appl. 1 (1) (1977) 69–83.

[13] M. Jirásek, Z.P. Bažant, Inelastic Analysis of Structures, John Wiley & Sons, New York, 2002.

[14] M. Jirásek, T. Zimmermann, Embedded crack model. Part II: Combination with smeared cracks, Int. J. Numer. Methods Engrg. 50 (2001) 1291–1305.

[15] J. Mazars, G. Pijaudier-Cabot, Continuum damage theory—application to concrete, J. Engrg. Mech. 115 (1989) 345–365.

[16] J.M. Melenk, I. Babuška, The partition of unity finite element method: basic theory and applications, Comput. Methods Appl. Mech. Engrg. 139 (1–4) (1996) 289–314.

[17] J.G.M. van Mier, Fracture Processes of Concrete, CRC Press, Inc., Boca Raton, Florida, 1997.

[18] N. Moës, T. Belytschko, Extended finite element method for cohesive crack growth, Engrg. Fract. Mech. 69 (2002) 813–833.

[19] N. Moës, J. Dolbow, T. Belytschko, A finite element method for crack growth without remeshing, Int. J. Numer. Methods Engrg. 46 (1) (1999) 131–150.

[20] S. Mohammadi, D.R.J. Owen, D. Peric, A combined finite/discrete element algorithm for delamination analysis of composites, Finite Elem. Anal. Des. 28 (1998) 321–336.

[21] J. Pamin, R. de Borst, Gradient-enhanced damage and plasticity models for plain and reinforced concrete, in: W. Wunderlich (Ed.), Proceedings of the European Conference on Computational Mechanics—ECCM'99, paper no. 636, Munich, 1999, Technical University of Munich, pp. 482–483.

[22] R.H.J. Peerlings, Enhanced damage modelling for fracture and fatigue, Ph.D. Thesis, Eindhoven University of Technology, 1999.

[23] R.H.J. Peerlings, R. de Borst, W.A.M. Brekelmans, M.G.D. Geers, Gradient-enhanced damage modelling of concrete fracture, Mech. Cohes.-Frict. Mater. 3 (1998) 323–342.

[24] R.H.J. Peerlings, R. de Borst, W.A.M. Brekelmans, M.G.D. Geers, Gradient-enhanced damage modelling of high-cycle fatigue, Int. J. Numer. Methods Engrg. 49 (2000) 1547–1569.

[25] R.H.J. Peerlings, R. de Borst, W.A.M. Brekelmans, J.H.P. de Vree, Gradient-enhanced damage for quasi-brittle materials, Int. J. Numer. Methods Engrg. 39 (1996) 3391–3403.

[26] G. Pijaudier-Cabot, Z.P. Bažant, Nonlocal damage theory, J. Engrg. Mech. 113 (1987) 1512–1533.

[27] E. Schlangen, Experimental and numerical analysis of fracture processes in concrete, Ph.D. Thesis, Delft University of Technology, 1993. Also published inHERON 38 (2) (1993) 3–117.

[28] I. Stakgold, Green's Functions and Boundary Value Problems, John Wiley & Sons, New York, 1979.

[29] M.G.A. Tijssens, L.J. Sluys, E. van der Giessen, Numerical simulation of quasi-brittle fracture using damaging cohesive surfaces, Eur. J. Mech. A/Solids 19 (5) (2000) 761–779.

[30] J.H.P. de Vree, W.A.M. Brekelmans, M.A.J. van Gils, Comparison of nonlocal approaches in continuum damage mechanics, Comput. Struct. 55 (1995) 581–588.

[31] G.N. Wells, Discontinuous modelling of strain localisation and failure, Ph.D. Thesis, Delft University of Technology, 2001.

[32] G.N. Wells, L.J. Sluys, A new method for modelling cohesive cracks using finite elements, Int. J. Numer. Methods Engrg. 50 (12) (2001) 2667–2682.

[33] G.N. Wells, L.J. Sluys, R. de Borst, Simulating the propagation of displacement discontinuities in a regularised strain-softening medium, Int. J. Numer. Methods Engrg. 53 (5) (2002) 1235–1256.

[34] X.-P. Xu, A. Needleman, Numerical simulations of fast crack growth in brittle solids, J. Mech. Phys. Solids 42 (1994) 1397–1434.

[35] C. Zhao, B.E. Hobbs, H.-B. Mühlhaus, A. Ord, A consistent point-searching algorithm for solution interpolation in unstructured meshes consisting of 4-node bilinear quadrilateral elements, Int. J. Numer. Methods Engrg. 45 (10) (1999) 1509–1526.